Constraining the denudation process in the eastern Sichuan basin, China using low-temperature thermochronology and vitrinite reflectance data from boreholes

Chuanqing Zhu*[1, 2, 3] Nansheng Qiu[1, 2] Yifeng Liu[4] Yao Xiao[1, 2] Shengbiao Hu[5]

[1] State Key Laboratory of Petroleum Resources and Prospecting, China University of Petroleum, Beijing 102249, China

[2] College of Geosciences, China University of Petroleum, Beijing 102249, China

[3] School of Geographic and Earth Sciences, University of Glasgow, Glasgow G12 8QQ, UK

[4] School of Earth Science and Engineering, Nanjing University, Nanjing 210023, China

[5] State Key Laboratory of Lithospheric Evolution, Institute of Geology and Geophysics, Chinese Academy of Sciences, Beijing 100029, China

*Corresponding author

Mobile: + 44- 07783838861

E-mail: zhucq@cup.edu.cn; chuanqing.zhu@glasgow.ac.uk

Abbreviated title: Constraining the denudation process in the Eastern Sichuan Basin

Abstract: The temperature history of samples and maximum paleogeothermal profiles of boreholes were reconstructed based on low-temperature thermochronology and vitrinite reflectance (Ro) data, and the results provide limits for the time scale and amount of uplift–denudation of the Eastern Sichuan Basin. The thermal history showed that the uplifting and cooling of eastern Sichuan basin began around the Late Cretaceous (approximately 100–80 Ma). The region had experienced a continuous cooling process from the Late Cretaceous until the present, with the geothermal gradient decreasing from 32–36 ℃/km to 20–23 ℃/km. The amount of denudation at the Puguang region in northeastern Sichuan was approximately 2.3 km, while that at southeastern Sichuan was 1.9 km, and the erosion thickness in the Eastern Sichuan fold belt that revealed via the field samples is 2.3±0.3-2.6±0.3 km. The northeastern Sichuan experienced sustained cooling with inconspicuous fluctuations, although the variation in the cooling rates was minor, while the thrust belt and the southeastern Sichuan basin presented 2-4 stages with different cooling rates. It may indicate that the episodic deformation of the detachment and thrust took place in the eastern Sichuan fold belt, and the Puguang area did not involve in mightily.

It may indicate that the eastern Sichuan fold belt experienced a complex structural evolution, characterized by episodic upliftings and deformations since Late Cretaceous, while a different and gentle deformation took place in the northeastern Sichuan basin.

Keywords: low-temperature thermochronology, vitrinite reflectance, thermal history, uplift–denudation, Eastern Sichuan Basin

1. Introduction

The Sichuan basin is one of China's large-scale basins rich in natural gas. Large gas fields are distributed in eastern Sichuan, including Puguang, Yuanba, and Longgang. In recent years, findings from the exploration and development of the Paleozoic layers have indicated great potential for deep-seated gas and shale gas in this basin (Li et al., 2011; Zeng et al., 2013). Uplift–denudation is closely related to the processes of hydrocarbon generation and expulsion, late-stage adjustments of oil and gas reservoirs, and the transformation and preservation of shale gas. Presently, the exposed strata in the Sichuan basin present the overall characteristic of being older and younger in the eastern and western regions, respectively. This indicates that various tectonic locations within the basin had undergone differential processes of denudation.

Researchers have placed emphasis on the uplift–denudation process there because it contains the obvious typical geomorphologies of a thrust–nappe zone, and got some insights on the limits for the time scale and amount involved in the basin's uplift–denudation (Deng et al., 2013; Hu et al., 2009; Liu et al., 2012; Lu et al., 2005; Mei et al., 2010; Qiu et al., 2008; Richardson et al., 2008; Shen et al., 2009; Tian et al., 2011; Tian et al., 2012; Wang et al., 2012; Yuan et al., 2010; Zhu et al., 2016a). Based on interpretations of the low temperature data including apatite fission track (AFT), apatite (U-Th)/He (AHe) and zircon (U-Th)/He (ZHe) analysis data, the tectonothermal evolution of east Sichuan basin has been reconstructed and discussed in details (i.e. Deng, et al., 2013; Shen et al., 2009; Tian et al., 2011; Tian et al., 2012).

The deformation and denudation of the Eastern Sichuan Basin were generally considered began from Cretaceous, while the time scale of the onset of uplifting was constrained by low temperature analysis to approximately 100-80 Ma as a whole (Deng et al., 2013; Shen et al., 2009; Tian, et al., 2011; Tian et al., 2012) or 135-65 Ma with regional differences (Wang et al., 2012). In contrast, the understandings of the erosion thickness were much more different, which included 2.0 km (Shen et al., 2009), 5.0 km (Tian et al., 2011), 1.5–2.7 km (Lu et al., 2005), and 2.2–2.9 km (Deng, et al., 2009), due to the variant adoptions in paleogeothermal gradients. In this study, low-temperature thermochronology and vitrinite reflectance (Ro) data were used combinedly to reconstruct both the temperature history of the samples and the plaeogeothermal gradients. Consequently, the result intuitively set the limits for the time scale and amount involved in the uplift–denudation of the Eastern Sichuan Basin. The accurately constrained denudation process is expected to provide evidence to the insights of the regional tectonics and structural evolution, and it also can affect the understanding of the hydrocarbon generation and accumulation process in the study area.

2. Geological setting

The Sichuan Basin is in the western margin of the Yangtze Craton, bounded on all sides by fold-thrust belts (FTB), i.e., the Micang Mt. and Daba Mt. belts in the north, the Longmen Mt. belt in the west, and the western Xiang-E (or called Hunan-Hubei) fold belt in the east. The main tectonic unit in the Eastern Sichuan Basin is a high steep tectonic belt belonging to the western belt of a Jura-type (or décollement) fold belt, which spans western Xiang-E and eastern Sichuan. This fold connects with the gentle fold belt of the Central Sichuan Basin to the west and abuts the Xuefeng uplift zone and Qinling orogenic zone to the east and north, respectively. It is basically an arcuate tectonic belt with a general north-northeast–northeast alignment, protrudes towards the northwest (Hu et al., 2009), and is bounded by the Qiyueshan Fault (Fig. 1). For the Sichuan Jura-type fold belt, the western and eastern belts consist of widely spaced anticlines (or comb folds) and widely spaced synclines, respectively (Hu et al., 2009; Mei et al., 2010; Wang et al., 2012).

Within the study area, the strata from the Paleozoic until Early Triassic were developed mainly from carbonate depositions of marine facies. From the Middle–Late Triassic onwards, a thick set of foreland basin deposition had formed. The deposition was affected by movements during the Caledonian, leading to the absence of the Devonian–Lower Carboniferous (Guo et al., 1996; Meng et al., 2005). The widely spaced anticlines exposed at the surface primarily consist of strata from the Triassic until Jurassic, and the type of fold structure is characterized by wide synclines and narrow anticlines. Both synclines and anticlines mostly appear as box folds with either flat bases or flat roofs. The center of the synclines is generally Jurassic, while the core of the anticlines is mostly exposed Triassic. The only exception is the middle section of the Huaying Mountain, where the core of the anticline consists of exposed Paleozoic (Hu et al., 2009). Cretaceous appear in localized areas within a small basin sited at the southeastern part of the study area. The differences between the various strata involved led to the general belief that the widely spaced anticlines found at the western part of the eastern Sichuan tectonic belt were mainly controlled by the Silurian décollement layer and belong to the typical Jura-type décollement fold belt (Hu et al., 2009; Yan et al., 2003), meanwhile the uplift and deformation processes in this belt are poorly constraint due to the lack of Cenozoic depositional records (Deng et al., 2013).

3. Database

The temperature interval between ~60 ℃ and 120 ℃ (e.g., Armstrong, 2005; Corrigan, 1993; Gallagher et al., 1995; Gleadow et al., 2015; Green et al., 1986; Ketcham et al., 2007; Ketcham, 2005; Laslett et al., 1987) is often referred to as the partial annealing zone (PAZ) of apatite fission track (Reiners et al., 2018). Natural samples and thermal modeling indicated substantial variations in the closure temperatures of (U–Th)/He systems for different minerals. The closure temperature of He in apatite is lower at 70-75 ℃ (Ehlers, et al., 2003; Floweers et al., 2009; Wolf et al., 1996); that of He in zircon was initially thought to be 140–160 ℃ (Reiners and Farley, 1999) but is currently believed to be 170–190 ℃ (Reiners, 2009; Reiners, 2002). When the retention time is varied, the closure temperature and partial retention zone of helium will also be different. Within geological time (1–100 Ma) and considering the thermal diffusion of helium inside zircon only, its partial retention zone is approximately 110–190 ℃ (Ketcham, 2005). The temperature interval which jointed by the different low-temperature thermal indicators, including AHe, AFT and ZHe, depending on the geothermal gradient, equate to a burial depth of ~3–7 km. Thus the low-temperature thermochronology can be used to reconstruct the cooling history of rocks as they approached the surface in response to erosion and tectonic processes.

3.1 Apatite fission track (AFT) and (U–Th)/He data

The results of the AFT analysis are summarized in Table 1. For all samples, their AFT age was younger than the stratigraphic age, which showed that the samples had undergone annealing. P(x^2) ≥ 5% for most of the samples, indicating that the age errors for individual particle samples were statistical errors. Since the AFT age was a single-component age, the pooled age could be used. For a few samples (such as the BB samples), the central age had to be used because P(x^2) < 5%, it indicates the AFT age was a multicomponent one, hence the central age was used.

It can be seen from Figs. 2 and 3 that a strong negative correlation exists between the AFT age and the embedded depth of the samples. Table 1 further reveals that the mean track length (MTL) exhibits a trend that decreases with the depth. However, this negatively correlated trend is not that strict compared to the relationship between the AFT age and the changes in the depth. After combining the distributional characteristics of the AFT lengths, it was determined that (i) for samples with a single-component AFT age, the track length distribution was mostly in the form of a single peak and (ii) for samples with a multicomponent AFT age (such as BB-9), the track length distribution contained multiple peaks.

The analytical results of apatite helium (AHe) and zircon helium (ZHe) thermochronology are summarized in Tables 2 and 3, respectively. With the exception of zircon samples from the shallow section of Borehole PG2, the test results for AHe and ZHe ages in this study were all smaller than the corresponding stratigraphic ages (Figs. 2 and 3). They indicate that the temperatures experienced by the samples had at least reached the range of the partial retention zone, which caused their ages to be reset.

3.2 Data profile of typical boreholes

The typical borehole profiles for the AFT, AHe, and ZHe ages are shown in Figs. 2 and 3 with the three types of paleothermal indicators having different closure (annealing) temperatures. The various strata gradually cooled after uplift–denudation, such that the younger overlying strata enter the ZHe, AFT, and AHe partial retention zones prior to the older underlying strata. The borehole profiles exhibited a decreasing trend with the depth for all three ages. On the basis of the same paleothermal standard, the shallower samples were older (for example, the ZHe ages of PG2-5 and PG2-6). This was mainly due to the presence of detrital particles that are older than the strata's deposition age. The paleothermal standard with a higher closure temperature would enter the partial retention zone before that with a lower closure temperature. Hence, for samples at the same embedded depth, the paleothermal standard with a higher closure temperature would be older. This meant that the ZHe, AFT, and AHe ages of each profile would be in a decreasing order.

Borehole Ro data from the oilfields were used in this study. For Borehole PG2, the samples were mainly concentrated at the approximate depth range of -1,200 to -3,500 m. The Ro value of the Jurassic–Triassic was approximately 1.2%–2.5%, with an overall increasing trend with the depth. However, the Ro values at depths of 1,200–2,500 m were concentrated at 1.2%–1.3%. Thus, it was inferred that at depths of 1,200–2,000 m, its test values tended to be high. The Ro data for Borehole G8 were fewer in number at depths of 1,800–2,600 m, the Ro values were between 1.0% and 1.5%.

4. Methods and Results

4.1 Methods

The temperature history of samples based on modeling using the low-temperature thermochronological data (i.e. AFT, AHe and ZHe) can serve as a reference for understanding burial and uplift–denudation processes. However, the burial and denudation process cannot be determined definitely based on the temperature paths, because the temperature gradients always changed due to the transitions of the tectonic background in the geological history. Other words, the burial history of samples may be very different to the temperature paths. As shown in Fig. 4, S1 experienced several stages of heating and cooling, and it seems the sample reached its maximum temperature at t_1 which much higher than that at t_3. Nevertheless, if we give different temperature gradients, for example, 36 ℃/km at t_1 and 25 ℃/km at t_2, the sample should be buried in the maximum depth at the later time. Both the two gradients are reasonable in a sedimentary basin.

The palaeotemperature gradient method (Bray et al., 1992; Duddy et al., 1991; Hu et al., 2007; O'Sullivan, 1999; Raza et al., 2009; Zhu et al., 2018), which estimates the palaeogeothermal gradient from the maximum palaeotemperature profile determined in a vertical sequence of samples from a borehole, can reveal both the evolution of the basin's thermal regime and the multiple-staged denudation. The theory and the workflow of the palaeotemperature gradient method to determine the maximum palaeotemperature gradient and the eroded thickness were stated by researchers (O'Sullivan, 1999; Hu et al., 2007; Zhu et al., 2018). As shown in Fig. 5, assuming the borehole section consists of two subsections (L1 and L2), actually two structural layers divided by unconformities. During the burial process, the two subsections experienced their maximum paleotemperature at different times (t1 and t2). Thus, in those maximum paleotemperature profiles, two paleotemperature profiles could be recognized, with the underlying subsection (L2) experiencing a much higher paleotemperature gradient than the overlying subsection (L1) before denudation (at time t2). In the same way, the paleotemperature gradient at t1 can be also determined from the paleotemperature indicators of L1.

The amount of denudation (E) could be estimated on the basis of the intercept (Ti) on the unconformity surface between (i) the paleogeothermal value during the maximum geothermal period (Ts) and (ii) the paleogeothermal profile. The equation is as follows:

$$E = (Ti - Ts)/(dT/dz)_m \quad (1)$$

where $(dT/dz)_m$ represents the maximum paleogeothermal gradient (G_m) when the paleogeothermal value was at the maximum.

More significantly, based on the understanding of the reconstructed paleogeothermal gradients, the thermal history modeling results that based on the low-temperature data can be reinterpreted. The denudation process, especially the erosion thickness can be determined via the combining of the paleotemperature and the paleo gradient. For example, in Fig.4, the erosion thickness for S2 from t_c to t_0 could be calculated use:

$$E = Zc - Z_0^2 = (Tc - Ts)/Gc - Z_0^2 \quad (2)$$

where Ts and Gc represent the paleo surface temperature and paleogeothermal gradient at t_c, Z_0^2 represents the buried depth at present which is surely knew for a borehole sample, for a surface sample, such as S1 showed in Fig.4, $Z_0^1 = 0$.

4.2 Results

4.2.1 Time scale limits for uplift–denudation: thermal history reconstructions for typical samples

Thermal history modelling for selected individual borehole samples was carried out combining AFT and AHe data together with regional geology constraints, thus, their present temperatures were determined by the buried depth and the measured temperature gradient (Lu et al., 2005; Xu et al., 2011). The temperature history modeling results for the AFT samples from Boreholes G8-1, PG2-5, and some field samples (BB-9, HD-2, DZ-4 and SZ-2) are shown in Figs. 6, 7, and 8, respectively. The modeling results of the typical samples showed that the samples began cooling ca. 90 Ma (80–100 Ma), with the cooling process continuing until the present. There was a definite amount of periodicity in the cooling of the samples, with various samples having different thermal histories. Most of the samples presented 2-4 stages of cooling: the earlier stages were gradual, but the later stages were rapid, compared to the PG-2 sample underwent sustained cooling with fluctuations, but there were only minor variations in the cooling rates.

The maximum paleotemperature intervals for all typical samples were within the AFT's partial annealing zone, so the thermal histories could be effectively constrained. At 90 Ma, G8-1 and PG2-5 reached the maximum paleo-temperatures of 120 ± 20 ℃ and 90 ± 10 ℃, respectively. Compared to the modeling results of the borehole samples, the field samples presented complex thermal histories, with more obvious rapid cooling since ~30Ma (BB-9) or later (within 20Ma).

4.2.2 Paleogeothermal gradient and amount of denudation

The reconstructed maximum paleo-temperature profiles of PG2 and G8 (Fig. 9) reflected the impacts of double actions on the study area, which lasted from the Late Cretaceous until the present; one was the uplift (denudation) effect, and the other was the basin cooling effect (declines in the paleogeothermal gradient and thermal flow). On the one hand, the slope of the maximum paleogeothermal profile (G_m) was greater than that of the present geothermal profile (G_p), indicating a reduction in the geothermal gradient from the past to the present. On the other hand, the paleo- and present geothermal profiles did not intersect on the present-day ground surface (the unconformity or denuded surface). In addition, the difference exceeded the possible differences of the surface temperatures between the paleo- and present. All of these demonstrate the existence of denudation.

After the maximum paleogeothermal profile had been reconstructed using both low-temperature thermochronology and Ro data, it was found that the maximum paleogeothermal gradient for the Puguang region (PG2) was 32.0 ℃/km, and the amount of denudation of the unconformity surface at the top of the Jurassic was 2.3 km. The maximum paleogeothermal gradient for southeastern Sichuan (G8) was higher (36.0 ℃/km), but the amount of denudation was smaller (1.9 km).

During the Late Cretaceous, the maximum paleo-temperature for BB-9, HD-2, DZ-4 and SZ-2 was 90 ± 5 ℃, 92 ± 10 ℃, 88 ± 5 ℃ and 86 ± 10 ℃ (Fig. 6). Using the paleogeothermal gradient of 36.0 ℃/km in the Southeast, and of 32 ℃/km in the Northeast, and the paleogeothermal value of 10 ℃, their maximum burial depth (or amount of denudation) was estimated to 2.5±0.1 km, 2.6±0.3 km and 2.4±0.1 km, 2.1±0.3 km, respectively, while the average denudation rate should be approximately 20-25m/Ma.

5. Discussion

This study's findings for the commencement time for uplift–denudation of the study area were generally consistent with that of previous research; that is, the Eastern Sichuan Basin began its uplift around the Late Cretaceous (approximately 100–80 Ma), during which the amount of uplift–denudation was substantial. However, there were differences in understanding regarding the actual cooling process during uplift and the exact amount of denudation. Shen et al. (2009) considered that the tectonic–thermal evolution process in northeastern Sichuan could be divided into three stages: (i) rapid uplift and cooling during 105–80 Ma, (ii) relative calm during 80–12 Ma, and (iii) rapid uplift and cooling since 12 Ma. This episodic cooling and uplifting styles are more similar as the samples in the thrust belt (i.e. the field samples, such as HD-2, DZ-4 and SZ-2). For the Puguang area (PG2-5) which is out of the thrust belt (see Fig. 1) presented a steadily and gently uplift or cooling because this area did not involve the detachment and thrust. That is, the difference of the temperature histories may indicate varies deformations in space and time of the Eastern Sichuan fold belt.

As mentioned before, there were substantial variations in the amount of denudation estimated by different researchers (Deng, et al., 2009; Deng, et al., 2013; Liu et al., 2012; Richardson, et al., 2008; Shen et al., 2009; Tian et al., 2011; Tian et al., 2012). These different estimates arose from the understanding of the paleogeothermal gradient. If the geothermal gradient for northeastern Sichuan within 100 Ma was assumed to be quite similar to the present gradient at 20 ℃/km, then the total amount of denudation for the region since the Late Cretaceous would be approximately 5 km, according to the temperature interval of cooling (~90 ℃). In reality, the basin’s thermal system was constantly changing during different stages of geological evolution. Thus, there would be limitations if the embedding and denudation histories were to be inferred directly from the samples’ temperature history. In this study, the reconstruction results based on the thermal histories of Ro and low-temperature thermochronological data were used as the basis to comprehensively establish the maximum paleogeothermal profile of the boreholes. Thus, the amount of denudation calculated in this study is more intuitive and accurate. However, the detailed denudation process, namely the evolution of the erosion rate since the Late Cretaceous to present cannot be constrained in detailed time scale, because the cooling can be caused by either denudation or the heat flow decrease. In general, the two causes are inseparable from each other, because the uplifting and deformation always give rise to denudation associated with heat flow decrease.

The Eastern Sichuan presents that uplifted earlier with more larger erosion thickness than the Western Sichuan depression (or is called a foreland basin) , which uplifted since Paleogene-Oligocene or even later (Liu et al., 2012; Liu et al., 2017; Yan et al., 2011; Yuan et al., 2010; Zhu et al., 2016b; Zhu et al., 2018) . Giving these details, a simple model was set to state the uplifting and denudation process since Late Cretaceous from the Eastern to the Western Sichuan basin (Fig. 10). It has been suggested that the uplifting and denudation of the eastern Sichuan basin were a result of pro-gressive northwestward propagation of the Yanshanian intra-continental deformation in Southern China due to the compression between the Kula-Pacific plate and the Eurasian plate (Wang, et al., 2010; Jin, et al., 2009; Yan et al., 2009; Yuan et al., 2010) and of the southwestward thrust-nappe tectonics from Dabashan intra-continental deformation (Shi et al., 2012). As shown in Fig.10, when the eastern Sichuan basin started to uplift and deformation at ~100 Ma, there was still a depression in the western Sichuan depression (or called Longmen Mt. foreland basin) and accepted deposits (Fig.10a), till the Cenozoic uplifting started (Fig.10b) due to the Late Cretaceous to Cenozoic compressional event in the Longmen Mt. FTB caused by the collision between India plate and Eurasia plate (Yan et al., 2011; Yuan et al., 2010).

6. Conclusion

The thermal history showed that the uplifting and cooling of eastern Sichuan basin began around the Late Cretaceous (approximately 100–80 Ma). Periodicities and regional variations were revealed during the uplift–denudation process. The northeastern Sichuan experienced sustained cooling with inconspicuous fluctuations, although the variation in the cooling rates was minor, while the thrust belt and the southeastern Sichuan basin presented 2-4 stages with different cooling rates. It may indicate that the episodic deformation of the detachment and thrust took place in the eastern Sichuan fold belt, and the Puguang area did not involve in mightily.

The region had experienced a continuous cooling process from the Late Cretaceous until the present, with the geothermal gradient decreasing from 32–36 ℃/km to 20–23 ℃/km. The amount of denudation of the unconformity surface at the top of the Jurassic was restored through the maximum paleogeothermal profile, which was jointly reconstructed using low-temperature thermochronological and Ro data. The amount of denudation at the Puguang region in northeastern Sichuan was approximately 2.3 km, while that at southeastern Sichuan was 1.9 km, and the erosion thickness in the Eastern Sichuan fold belt that revealed via the field samples is 2.1±0.3-2.6±0.3km. The result shows that the erosion thickness is larger in the eastern basin that the uplifting began earlier than that in the western basin, where the uplifting began in a later time.

ACKNOWLEDGMENTS: The study was supported by the National Science Foundation of China (Grant No. 41772248, 41690013) "National Science and the Technology Major Project" of China (Grant No. 2017ZX05008004). The first author is grateful to the Chinese

Scholarship Council (CSC) for supporting him stay in the University of Glasgow as a sponsored researcher.

REFERENCES

Armstrong, P.A., 2005. Thermochronometers in Sedimentary Basins. Reviews in Mineralogy and Geochemistry, 58 (1): 499-525.

Bray, R. J., Green, P. F., Duddy, I. R., 1992. Thermal history reconstruction using apatite fission track analysis and vitrinite reflectance: a case study from the UK East Midlands and Southern North Sea. Geological Society, London, Special Publications, 67, 3-25.

Corrigan, J., 1991. Inversion of apatite fission track data for thermal history information. Journal of Geophysical Research, 96: 347-360.

Deng, B., Liu, S.G., Liu, S., Li, Z.W., Zhao, J.C. 2009. Restoration of exhumation thickness and its significance in Sichuan basin, China. Journal of Chengdu University of Technology (Science & Technology Edition) 36, 675–686.

Deng, B., Liu, S. G., Li, Z. W., Jansa, L. F., Liu, S., Wang, G. Z., Sun, W. 2013. Differential exhumation at eastern margin of the Tibetan Plateau, from apatite fission-track thermochronology. Tectonophysics, 591(591), 98-115.

Duddy, I. R., Green, P. F., Lastett, G. M., 1988. Thermal annealing of fission tracks in apatite, 3. Aariable temperature behaviour. Chemical Geology, 73: 25-38.

Ehlers, T.A., Farley, K.A., 2003. Apatite (u–th)/he thermochronometry: methods and applications to problems in tectonic and surface processes. Earth & Planetary Science Letters, 206(1–2), 1-14.

Farley, K. A., Wolf, R. A., Silver, L. T., 1996. The effects of long alpha-stopping distances on (U-Th)/He ages. Geochimica Et Cosmochimica Acta, 60(21), 4223-4229.

Flowers, R.M., Ketcham, R.A., Shuster, D.L., Farley, K.A. 2009. Apatite (U-Th)/He thermochronometry using a radiation damage accumulation and annealing model. Geochim. Cosmochim. Acta, 73, 2347–2365.

Gallagher, K., 1995. Evolving temperature histories from apatite fission-track data. Earth Planet Science Letters, 136: 421-435.

Gleadow, A., Harrison, M., Kohn, B., Lugo-Zazueta, R., Phillips, D. 2015. The fish canyon tuff: a new look at an old low-temperature thermochronology standard. Earth & Planetary Science Letters, 424, 95-108.

Green, P. F., Duddy, I. R., Gleadow, A. J. W., Tingate, P. R., Laslett, G. M., 1986. Thermal annealing of fission tracks in apatite : 1. a qualitative description. Chemical Geology Isotope Geoscience, 59(4), 237-253.

Guo, Z.W., Deng, K.L., Han, Y.H., Liu, Y.K., Yin, J.T., Wang, Q.G., Liang, E.Y., Li, G.J., Chen, Z.G., Liu, Z.Z., Wu, C.S., Zhao, Z.J., 1996. The formation and development of Sichuan Basin. Geological Publishing House, Beijing.

Hu, S. B., Fu, M. X., Yang, S. C., et al., 2007. Palaeogeothermal response and record of Late Mesozoic lithospheric thinning in the eastern North China Craton. in: Zhai M G, Windley B F, Kusky T M, et al. (eds) Mesozoic Sub-Continental Lithospheric Thinning Under Eastern Asia. Geological Society, London, Special Publications, 280: 267–280.

Hu, S. Q., Zhu, G., Liu, G. S., Zhang, B. L. 2009. The folding time of the eastern Sichuan Jura-type fold belt: evidence from unconformity. Geological Review, 55(1), 32-42.

Jin, Z. J., Yuan, Y. S., Liu, Q. Y., Wo, Y. J. 2013. Controls of Late Jurassic-Early Cretaceous tectonic event on source rocks and seals in marine sequences, south China. Science Chin: Earth Sciences, 56(2), 228-239.

Ketcham, R. A. 2005. Forward and inverse modeling of low temperature thermochronometry data. Reviews in Mineralogy and Geochemistry, 58: 275-314.

Ketcham, R. A., Carter, A., Donelick, R. A., et al., 2007. Improved modeling of fission-track annealing in apatite. Am. Mineral., 92: 799-810.

Laslett, G. M., Green, P. F., Duddy, I. R., Gleadow, A. J. W., 1987. Thermal annealing of fission tracks in apatite 2. a quantitative analysis. Chemical Geology Isotope Geoscience, 65(1), 1-13.

Li, W., Zhang, Z. J., Dang, L. R. 2011. Depositional systems and evolution of the upper carboniferous Huanglong formation in the eastern Sichuan basin. Petroleum Exploration & Development, 38(4), 400-409.

Liu, S. G., Deng, B., Li, Z. W., Sun, W. 2012. Architecture of basin-mountain systems and their influences on gas distribution: a case study from the Sichuan basin, south China. Journal of Asian Earth Sciences, 47(1), 204-215.

Liu, S.G., Deng, B., Jansa, L., Li, Z.W., Sun, W., Wang, G.Z., Luo, Z.L., Yong, Z.Q., 2017. Multi-stage basin development and hydrocarbon accumulations: a review of the Sichuan basin at eastern margin of the Tibetan Plateau. Journal of Earth Science, doi: 10.1007/s12583-017-0904-8.

Lu, Q. Z., Hu, S. B., Guo, T. L., Li, Z. P. 2005. The background of geothermal field for the formation of abnormal high pressure in northeastern Sichuan basin. Chinese Journal of Geophysics, 48(5), 1184-1191.

Mei, L. F., Liu, Z. Q., Tang, J. G., Shen, C. B., Fan, Y. F. 2010. Mesozoic intra-continental progressive deformation in western Hunan-Hubei-eastern Sichuan provinces of China: evidence from apatite fission track and balanced cross-section. Earth Science, 35(2), 161-174.

Meng, Q. R., Wang, E., Hu, J. M., 2005. Mesozoic sedimentary evolution of the northwest sichuan basin: implication for continued clockwise rotation of the south china block. Geological Society of America Bulletin, 117(3), 396-410.

O'Sullivan, P. B., 1999. Thermochronology, denudation and variations in palaeosurface temperature: A case study from the North Slope foreland basin, Alaska. Basin Research, 11: 191–204.

Qiu, N. S., Qin, J. Z., Brent, M., Wang, J., Tenger, Zhen, L. J. 2008. Tectonothermal evolution of the northeastern Sichuan basin: constraints from apatite and zircon(u-th)/he ages and vitrinite reflectance data. Geological Journal of China Universities, 14(2): 223-230.

Raza, A., Hill, K. C., Korsch, R. J. 2009. Mid-Cretaceous uplift and denudation of the Bowen and Surat Basins, eastern Australia: relationship to Tasman Sea rifting from apatite fission-track and vitrinite-reflectance data. Australian Journal of Earth Sciences, 56(3): 501-531.

Reiners, P. W., 2009. Nonmonotonic thermal histories and contrasting kinetics of multiple thermochronometers. Geochimica Et Cosmochimica Acta, 73(12), 3612-3629.

Reiners, P. W., 2002. Temporal-compositional trends in intraplate basalt eruptions: implications for mantle heterogeneity and melting processes. Geochemistry Geophysics Geosystems, 3(2), 1-30.

Reiners, P.W., Carlson, R.W., Renne, P.R., Cooper, K.M., Granger, D. E., McLean, N.M., Schoene, B., 2018. Geochronology and Thermochronology. John Wiley & Sons Ltd, Hoboken.

Richardson, N. J., Densmore, A. L., Seward, D., Fowler, A., Wipf, M., Ellis, M. A., 2008. Extraordinary denudation in the sichuan basin: insights from low‐temperature thermochronology adjacent to the eastern margin of the tibetan plateau. Journal of Geophysical Research Solid Earth, 113(B4), -.

Shen, C. B., Mei, L. F., Xu, S. H. 2009. Fission track dating of Mesozoic sandstones and its tectonic significance in the eastern Sichuan basin, China. Radiation Measurements, 44(9), 945-949.

Shi, W., Zhang, Y., Dong, S., Hu, J., Wiesinger, M., Ratschbacher, L., 2012. Intra-continental dabashan orocline, southwestern qinling, central china. Journal of Asian Earth Sciences, 46(6), 20-38.

Sweeney, J. J., Burnham, A. K., 1990. Evaluation of a simple model of vitrinite reflectance based on chemical kinetics. AAPG Bulletin, 74: 1559-1570.

Tian, Y. T., Zhu, C. Q., Ming, X. U., Song, R., Kohn, B. P., Hu, S. B., 2011. Post-Early Cretaceous denudation history of the northeastern Sichuan basin: constraints from low-temperature thermochronology profiles. Chinese Journal of Geophysics- Chinese Edition, 54(3), 807-816.

Tian, Y. T., Qiu, N. S., Kohn, B. P., Zhu, C. Q., Hu, S. B., Gleadow, A. J. W., McInnes, B. I. A. 2012. Detrital zircon (u–th)/he thermochronometry of the Mesozoic Daba Shan foreland basin, central China: evidence for timing of post-orogenic denudation. Tectonophysics, 570–571, 65–77.

Wang, P., Liu, S. F., Gao, T. J., Wang, K. 2012. Cretaceous propagation of the eastern Sichuan arcuate fold‐thrust belt in three dimensions: insights from AFT analysis. Chinese Journal of Geophysics- Chinese Edition, 55(5), 1662-1673.

Wolf, R. A., Farley, K. A., Silver, L. T., 1996. Helium diffusion and low-temperature thermochronometry of apatite. Geochimica Et Cosmochimica Acta, 60(21), 4231-4240.

Yan, D.P., Zhou, M.F., Li, S.B., Wei, G.Q., 2011. Structural and geochronological constraints on the Mesozoic-Cenozoic tectonic evolution of the Longmen Shan thrust belt, eastern Tibetan Plateau. Tectonics, 30, TC6005, doi: 10.1029/2011TC002867

Yan, D. P., Zhang, B., Zhou, M. F., Wei, G., Song, H. L., Liu, S. F., 2009. Constraints on the depth, geometry and kinematics of blind detachment faults provided by fault-propagation folds: an example from the mesozoic fold belt of south china. Journal of Structural Geology, 31(2), 150-162.

Yan, D. P., Zhou, M. F., Song, H. L., Wang, X. W., Malpas, J., 2003. Origin and tectonic significance of a mesozoic multi-layer over-thrust system within the Yangtze block (south China). Tectonophysics, 361(3), 239-254.

Yuan, Y. S., Sun, D. S., Zhou, Y., Wang, X. W., Li, S. J., Zhang, R. Q., Wo, Y. J. 2010. Determination of onset of uplifting for the Mid-Upper Yangtze area since Indosinian event. Chinese Journal of Geophysics, 53(53), 455-461.

Zeng, W. T., Ding, W. L., Zhang, J. C., Zhang, Y. Q., Guo, L., Jiu, K., Li, Y. F. 2013. Fracture development in Paleozoic shale of Chongqing area (South China). Part two: Numerical simulation of tectonic stress field and prediction of fractures distribution. Journal of Asian Earth Sciences, 75(8), 267-279.

Zhu, C. Q., Qiu, N. S., Cao, H. Y., Rao, S., Hu, S. B. 2016a. Paleogeothermal reconstruction and thermal evolution modeling of source rocks in the puguang gas field, northeastern Sichuan basin. Journal of Earth Science, 27(5): 796-806.

Zhu, C. Q., Rao, S., Hu, S. B. 2016b. Application of illite crystallinity for paleo-temperature reconstruction: a case study in the western Sichuan basin, SW China. Carpathian Journal of Earth and Environmental Sciences, 11(2): 599-608.

Zhu, C. Q., Hu, S. B., Qiu, N. S., Jiang, Q., Rao, S., Liu, S. 2018. Geothermal constraints on Emeishan mantle plume magmatism: paleotemperature reconstruction of the Sichuan Basin, SW China. International Journal of Earth Sciences, 107(1): 71-88.

Table 1 Apatite fission track data from the field and boreholes in the Eastern Sichuan Basin*

Sample	Coordinate	Elevation (m)	Depth (m)	strata	Ng	ρ_s (10^5/cm^2) (Ns)	ρ_i (10^5/cm^2) (Ni)	ρ_d (10^5/cm^2) (Nd)	P(χ^2) (%)	Age (Ma) (±1σ)	L(μm) (NL)
BB-8	29°48′09″ N 106°28′15″ E	208		T_3x	28	1.97 (317)	15.772 (2538)	16.535 (8116)	0.4	42±4	12.4±2.2(105)
BB-9	29°48′04″ N 106°28′18″ E	209		T_3x	28	2.214 (765)	12.862 (4444)	16.757 (8116)	0.3	54.5±4.1	12.4±2.1(103)
BB-13	29°46′58″ N 106°29′27″ E	207		J_2s	19	2.443 (97)	22.788 (905)	16.976 (8116)	4.0	39.1±5.2	12.4±2.5(13)
DZ-4	30°46′19″ N 107°08′50″ E	433		J_2x	28	4.574 (223)	22.52 (1098)	17.197 (8116)	40.5	73.0±6.4	10.9±2.1(47)
DZ-14	30°46′04″ N 107°06′37″ E	843		T_3x	3	4.723 (52)	35.06 (386)	17.417 (8116)	80.8	48.0±7.0	11.5±2.7(8)
DZ-12	30°45′55″ N 107°07′24″ E	706		T_3x	21	0.530 (145)	1.0129 (281)	14.458 (12459)	100.00	77.9±9.3	11.02±1.94(24)
HD-1	31°01′54″ N 107°09′16″ E	262		T_3x	20	0.458 (163)	0.985 (366)	14.165 (12459)	98.56	65.9±7.5	12.02±1.23(24)
HD-2-a	31°01′12″ N 107°11′35″ E	295		T_3x	21	11.536 (133)	19.833 (228)	14.092 (12459)	82.04	85.7±10.8	11.44±1.35(16)
HD-2-b	31°01′12″ N 107°11′35″ E	295		T_3x	21	2.395 (133)	4.579 (250)	14.678 (12459)	100.00	81.5±10.1	11.67±1.69(22)
HD-2**	31°01′12″ N 107°11′35″ E	295		T_3x	42				92.00	81.9±17.8	11.57±1.58(38)
SZ-2	29°58′08″ N 108°0′43″ E	836		J_2s	19	2.789 (128)	5.352 (239)	14.605 (12459)	99.95	81.6±10.3	11.89±1.83(30)
G8-1	28°21′12″ N 105°58′17″ E		-1257.7	J_2sn	20	3.424 (612)	24.39 (4360)	16.23 (3041)	41.56	44.2±2.2	12.26±1.96(72)
G8-2	28°21′12″ N 105°58′17″ E		-1829.2	J_2sn	21	3.777 (321)	32.19 (2736)	16.13 (3041)	60.8	34.6±2.7	11.46±1.5(53)
G8-4	28°21′12″ N 105°58′17″ E		-2190.2	T_3x	25	2.763 (189)	45.72 (3128)	16.04 (3041)	99.01	18.9±1.5	12.26±1.5(99)
G8-5	28°21′12″ N 105°58′17″ E		-2475.7	T_3x	25	2.146 (141)	30.48 (2003)	15.95 (3041)	86.74	21.9±1.9	
PG2-2	31°31′16″ N		-3025.9	T_3x	20	1.758	44.29	16.48	99.9	12.7±1.9	

	107°47′19″ E				(50)	(1260)	(3125)			
PG2-3	31°31′16″ N 107°47′19″ E	-3247.1	T_3x	21	0.667 (65)	17.54 (1710)	15.39 (3041)	96.2	11.4±1.5	
PG2-4	31°31′16″ N 107°47′19″ E	-3415.5	T_3x	20	0.761 (44)	32.78 (1895)	14.80 (2988)	77.7	6.7±1.0	
PG2-5	31°31′16″ N 107°47′19″ E	-370.0	J_2sn	21	4.82 (257)	19.82 (1057)	14.92 (2988)	83.8	70.2±5.1	12.10±1.8(104)
PG2-6	31°31′16″ N 107°47′19″ E	-1590.0	J_2x	22	4.903 (182)	38.69 (1436)	15.04 (2988)	99.7	37.0±3.0	12.0±1.65(106)

*Notes: Ng= Number of dated grains, Ns = Number of counted spontaneous tracks; Ni= Number of counted induced tracks; ρs = density of spontaneous tracks; ρi = density of induced tracks; Nd = Number of tracks on standard glass; ρd = Density of tracks on standard glass; L = Mean track length; NL= Number of measured track lengths. The AFT data of PG2 and G8 sourced from Tian et al. (2011) and Zhu et al. (2016a). The ages of the borehole samples (from G8 and PG2) which were analyzed in the University of Melbourne calculated using a zeta of 389.3 ± 5.0 for dosimeter glass Corning-5, while the ages of the field samples BB-8, BB-9, BB-13, DZ-4 and DZ-14 which were analyzed in China University of Geosciences, Beijing using a zeta of 410.4 ± 17.6, and the samples HD-1, HD-2, DZ-12 and SZ-2 which were analyzed in China University of Petroleum, Beijing using a zeta of 210 ± 13.0.

**Note: The data of HD-2 was combined from the AFT ages and lengths of HD-2-a and HD-2-b.

Table 2 AHe data from boreholes G8 and PG 2 in the Eastern Sichuan Basin*

Sample No.	Mass [g]	U [ppm]	Th [ppm]	^{4}He [ncc]	Th/U	F_T	Corrected age [Ma]	1σ	Age of sample[Ma]
PG2-5	0.0013	94.4	214.3	0.464	2.27	0.65	31.0	1.9	46.4±14.1
	0.0021	5.7	21.9	0.125	3.87	0.71	58.6	3.6	
	0.0013	18.9	21.5	0.121	1.14	0.66	49.6	3.1	
PG2-6	0.0025	27.6	34.8	0.122	1.26	0.68	16.2	1.0	15.0±2.9
	0.0046	7.8	30.3	0.070	3.87	0.73	11.6	0.7	
	0.0020	10.8	37.2	0.057	3.44	0.70	16.8	1.0	
	0.0061	32.6	97.2	0.499	2.98	0.65	18.5	1.1	
G8-1	0.0082	1.7	8.2	0.128	4.86	0.81	41.0	2.5	31.9±8.4
	0.0177	62.4	80.3	4.403	1.29	0.83	30.2	1.9	
	0.0063	692.9	666.4	12.775	0.96	0.80	24.4	1.5	
G8-2	0.0059	21.0	26.4	0.067	1.26	0.75	4.5	0.3	6.8±3.2
	0.0078	7.1	10.2	0.066	1.44	0.80	9.0	0.6	

*Note: Results were analysed in the University of Melbourne, F_T is the α-ejection correction (Farley et al., 1996).

Table 3 ZHe data from boreholes G8 and PG 2 in the Eastern Sichuan Basin*

Sample No.	Mass [g]	U [ppm]	Th [ppm]	Corrected gas[ncc]	Th/U	F_T	Corrected age [Ma]	1σ	Age of Sample [Ma]
PG2-2	0.0032	45.4670	48.7521	2.687	1.07	0.73	118.7	7.3	120.6±7.7
	0.0040	65.0621	73.8919	4.901	1.14	0.74	122.3	7.6	
PG2-4	0.0123	115.5376	66.0679	34.363	0.57	0.82	174.1	10.8	
	0.0076	777.4734	333.0530	96.291	0.43	0.78	120.2	7.4	
PG2-5	0.0037	294.3509	58.0478	23.324	0.20	0.74	166.2	10.3	
	0.0062	248.0350	222.9136	45.255	0.90	0.77	195.1	12.1	
PG2-6	0.0036	323.3178	666.7065	40.457	2.06	0.73	187.7	11.6	186.2±10.7
	0.0058	173.5035	138.2995	15.932	0.80	0.77	184.6	11.4	
G8-1	0.0074	237.6661	256.8828	22.181	1.08	0.79	82.3	5.1	
	0.0139	120.0928	123.4776	9.723	1.03	0.82	38.3	2.4	
G8-5	0.0034	314.2050	108.1709	9.422	0.34	0.75	66.2	4.1	
	0.0036	311.9019	266.2882	5.197	0.85	0.74	31.6	2.0	

*Note: Results were analysed in the University of Melbourne, F_T is the α-ejection correction (Farley et al., 1996). The data of samples from borehole PG2 sourced from Tian et al. (2012).

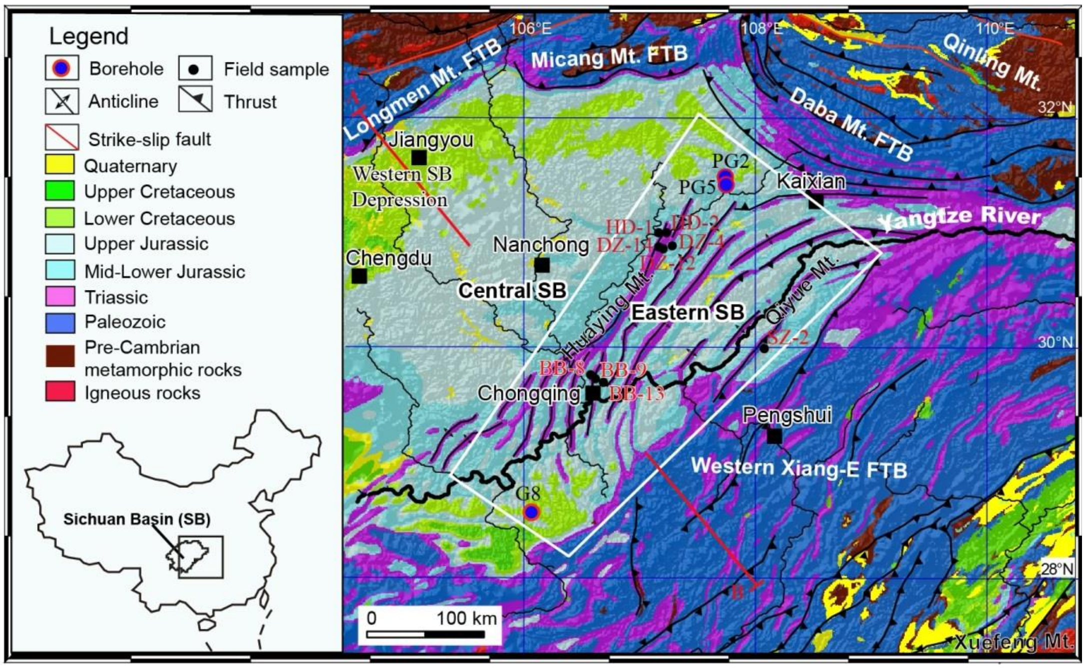

Fig. 1 Geological map of the Eastern Sichuan Basin indicating the borehole locations and field sampling points (Geological map modified from Tian et al., 2011)

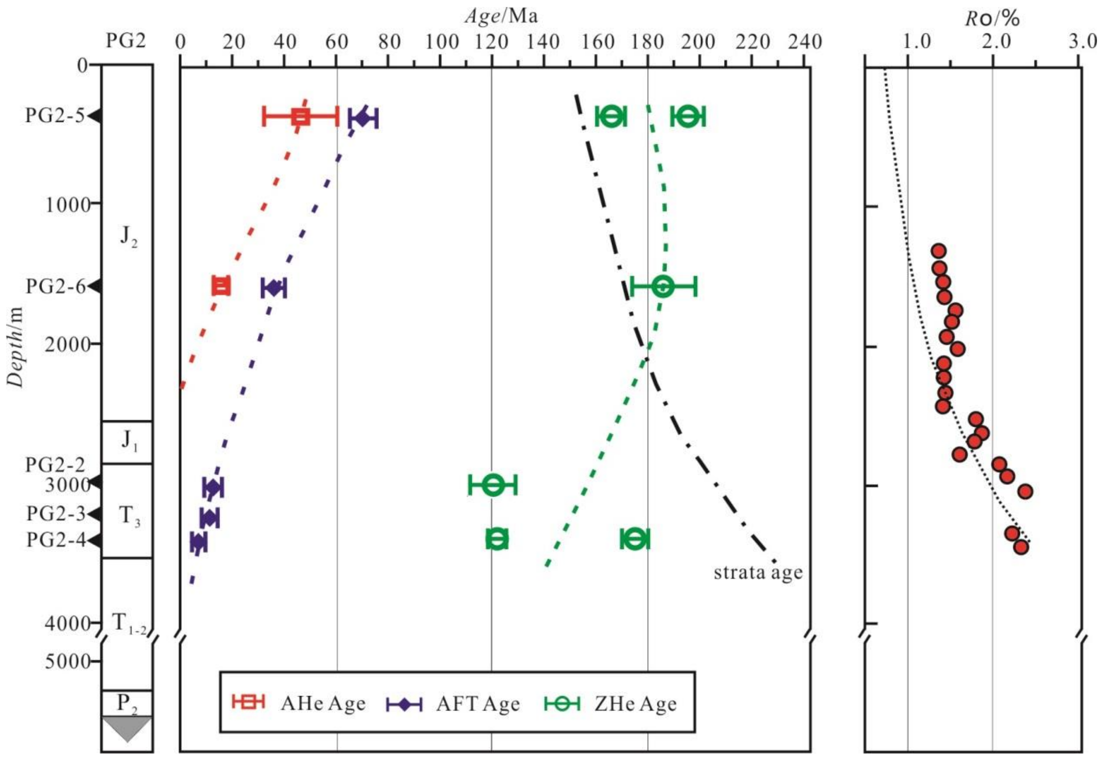

Fig. 2 AHe, ZHe, AFT age profiles and the Ro data of Borehole PG2. The Ro data sourced from the exploration branch, SINOPEC.

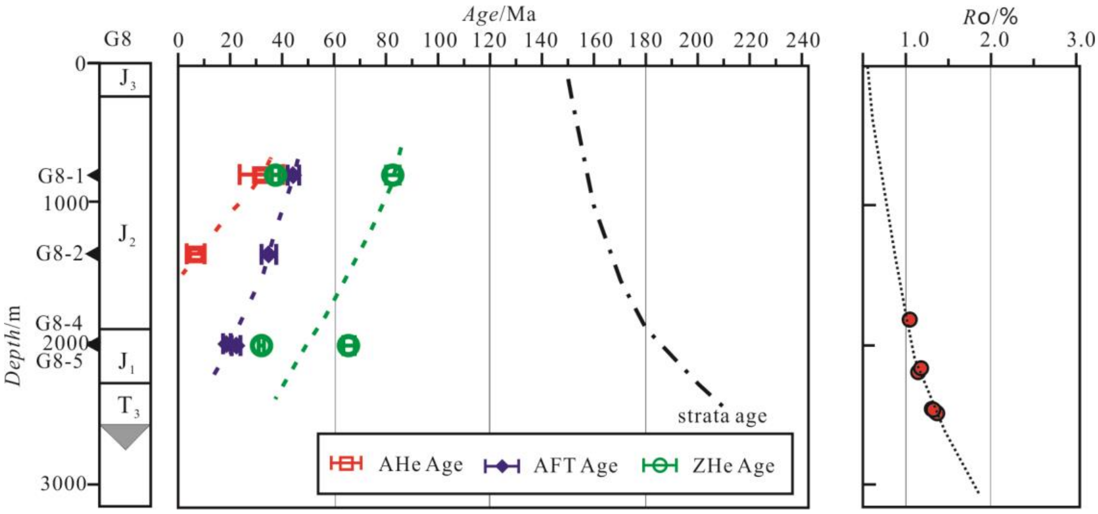

Fig. 3 AHe, ZHe, AFT age profiles and the Ro data of Borehole G8. The Ro data sourced from the exploration branch, SINOPEC.

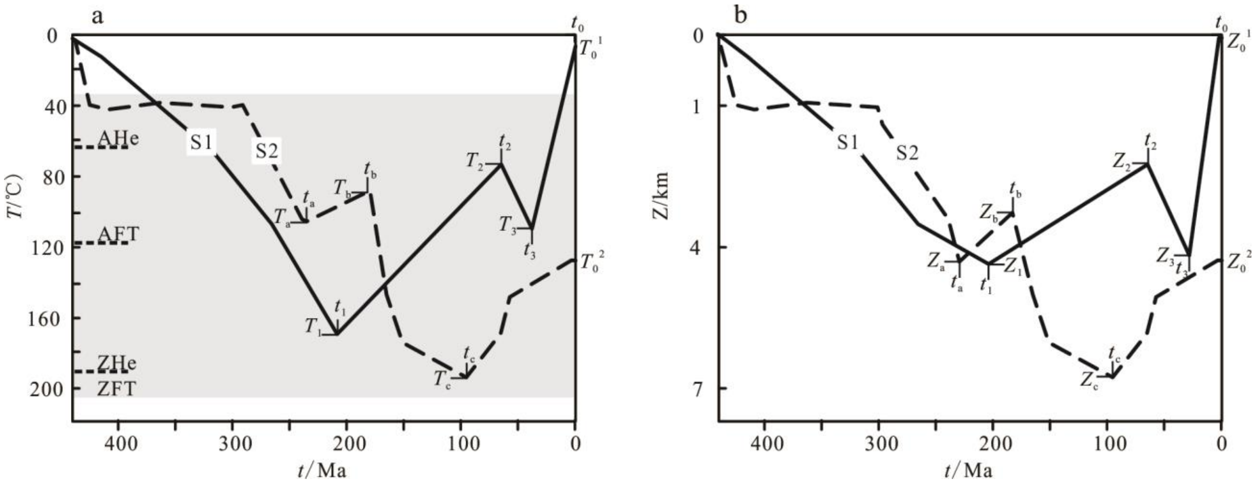

Fig. 4 Sketch map showed the uncertainty and multiplicity of solution for denudation from the temperature paths. Panel (a) showed the temperature paths of two samples, S1 indicate the surface sample, while S2 is from borehole. Panel (b) showed one of the possible solutions for burry and denudation.

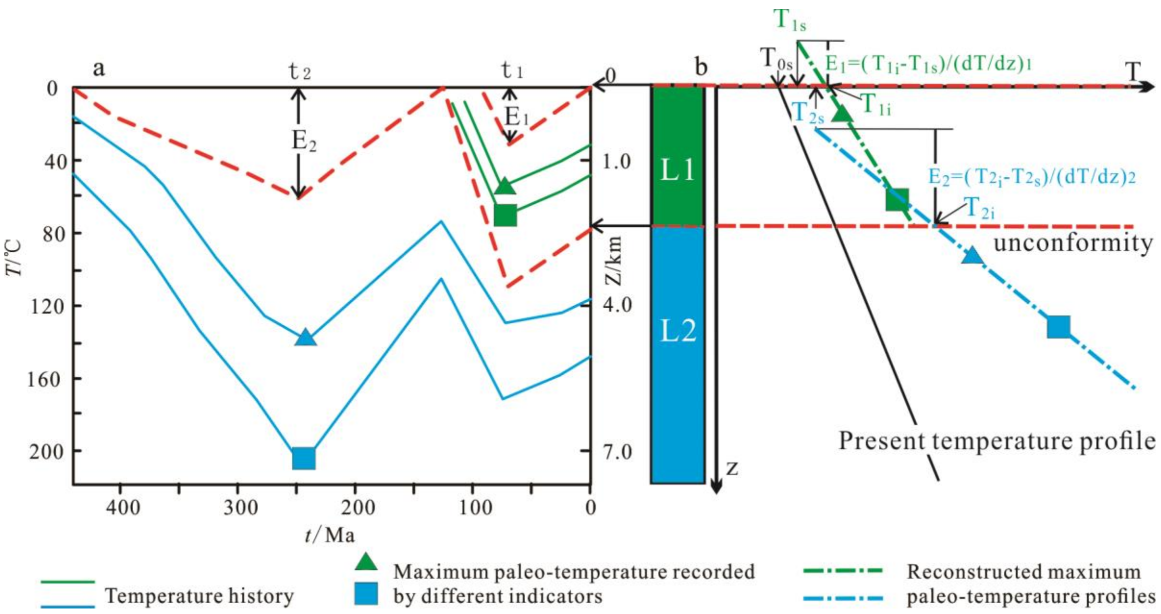

Fig. 5 Schematic diagrams show how the plaeo-temperatures recorded by geothermal indicators (left panel) and methods to determine the maximum palaeotemperature gradient and the eroded thickness (right panel) (after O'Sullivan, 1999; Hu et al., 2007; Zhu et al., 2018). The profiles provide distinguished palaeotemperature gradients (dT/dz), and then the thickness (Ei) of the removed section on the corresponding unconformities can be obtained by dividing the difference between the surface temperature (Ts) and the intercept of the palaeotemperature profile (Ti) at the top unconformity by the estimated palaeotemperature gradient.

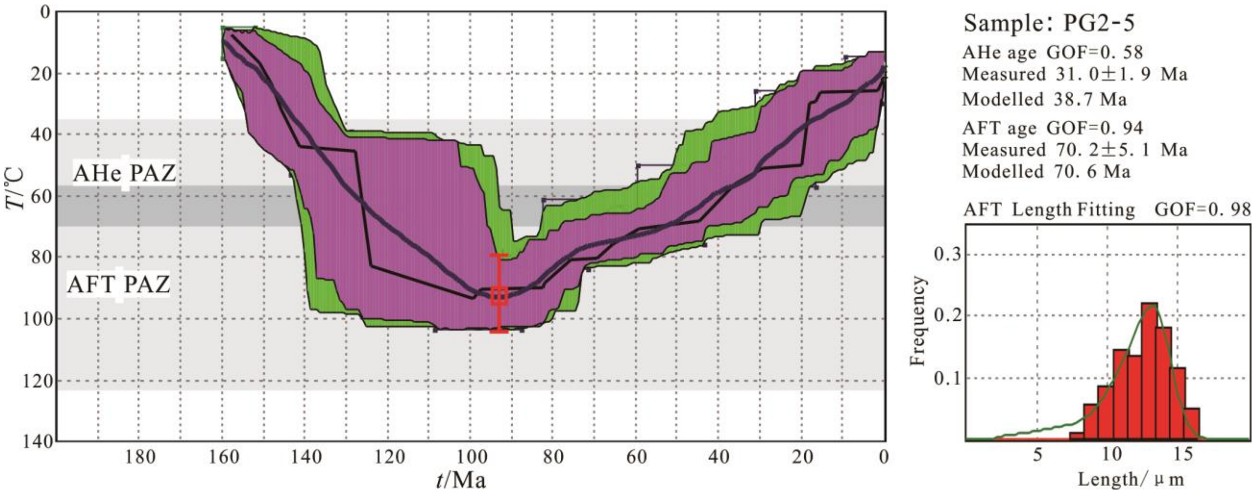

Fig. 6 Thermal history modeled for PG2-5 based on AFT and AHe data. The multi-kinetic annealing model (Ketcham et al., 2007) was used for AFT modelling, while the AHe data were modelled using the radiation damage accumulation and annealing model (Flowers et al., 2009). Total of 10000 paths have been modeled using the Monte Carlo method via the HeFTy software package (Ketcham, 2005) for each individual sample. The inversion results are a series of possible or equivalent thermal history paths that constitute a probability-distribution belt. The width and dispersion of the belt depend on the complexity of its thermal history. A more complex thermal history exhibits a wider distribution belt and greater uncertainty. Green regions indicate the envelopes of "accepted traces" (0.05 ≤ GOF < 0.5), and purple regions indicate the envelopes of "good traces" (0.5 ≤ GOF ≤ 1.0). Blue bold line in each result indicates the mean of "good traces." The GOFs (goodness of fit) of these results were listed on the up left panel, and the green curves indicate the fit of the AFT length distribution on the right bottom panel. This statement is also suitable for Fig.7 and Fig.8.

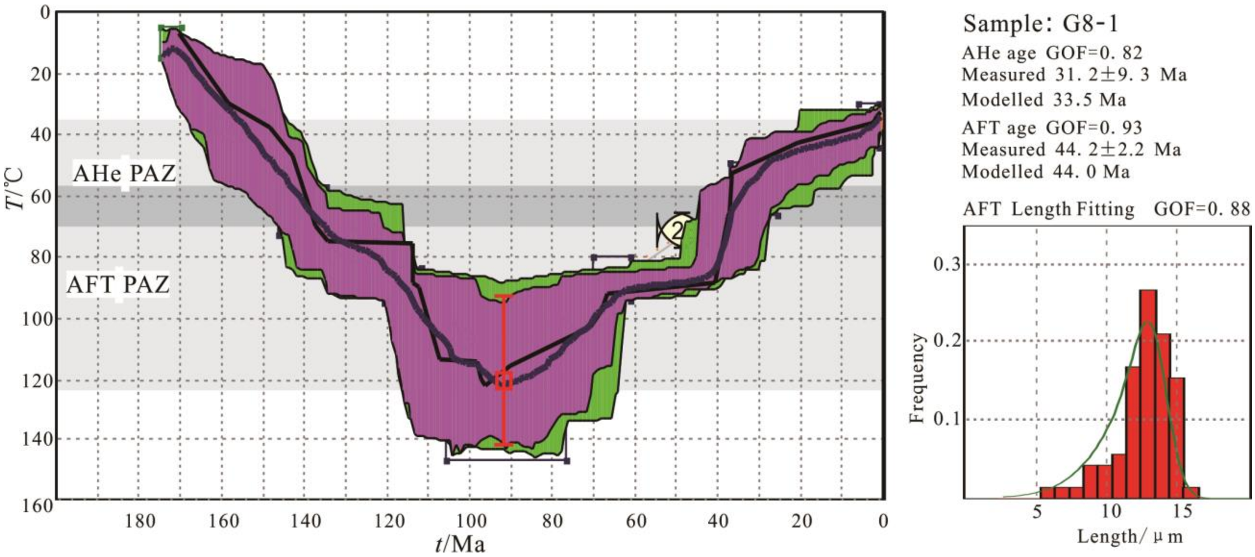

Fig. 7 Thermal history modeled for G8-1 based on AFT and AHe data

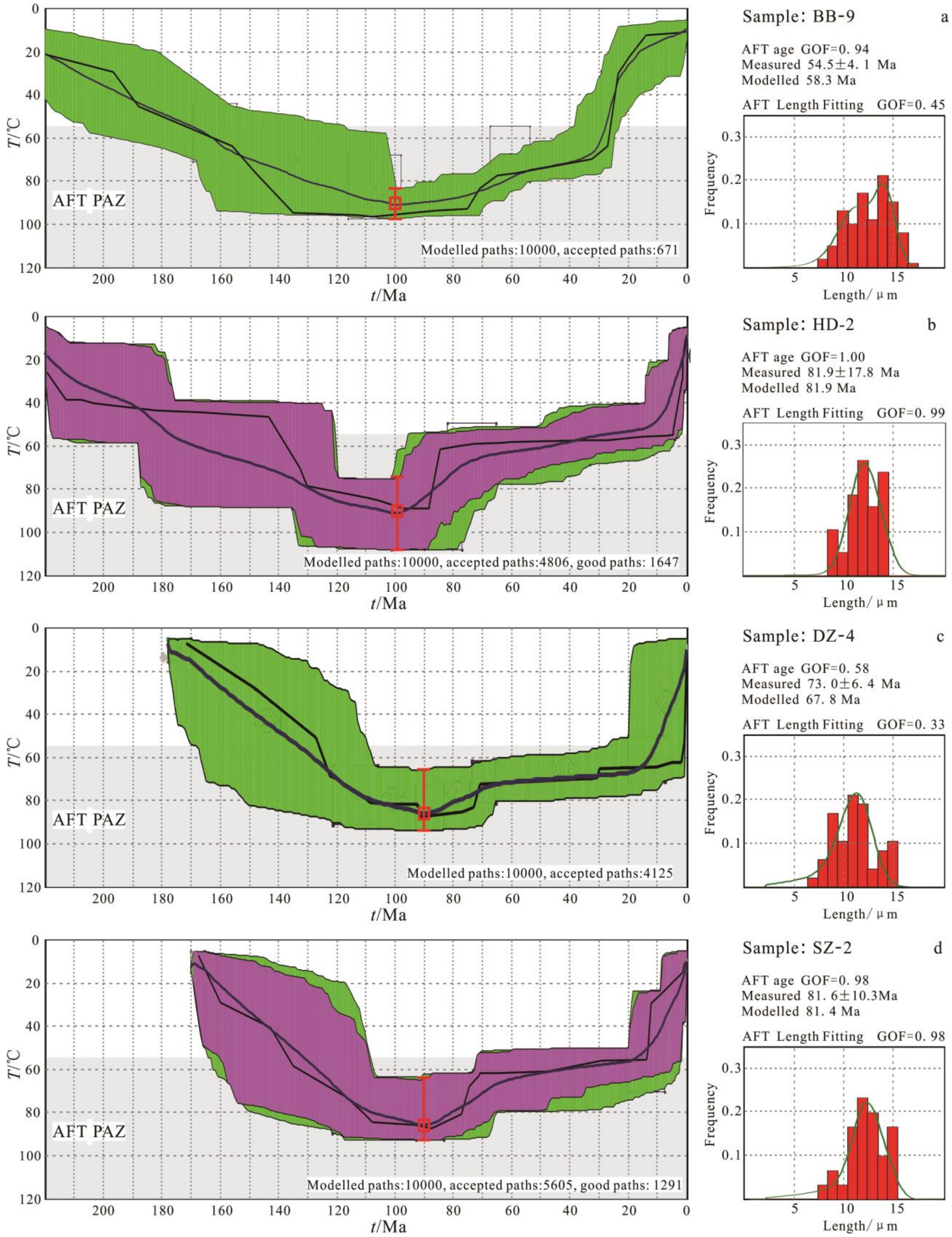

Fig. 8 Thermal history modeled for the field samples (BB-9, HD-2, DZ-4 and SZ-2) based on AFT data

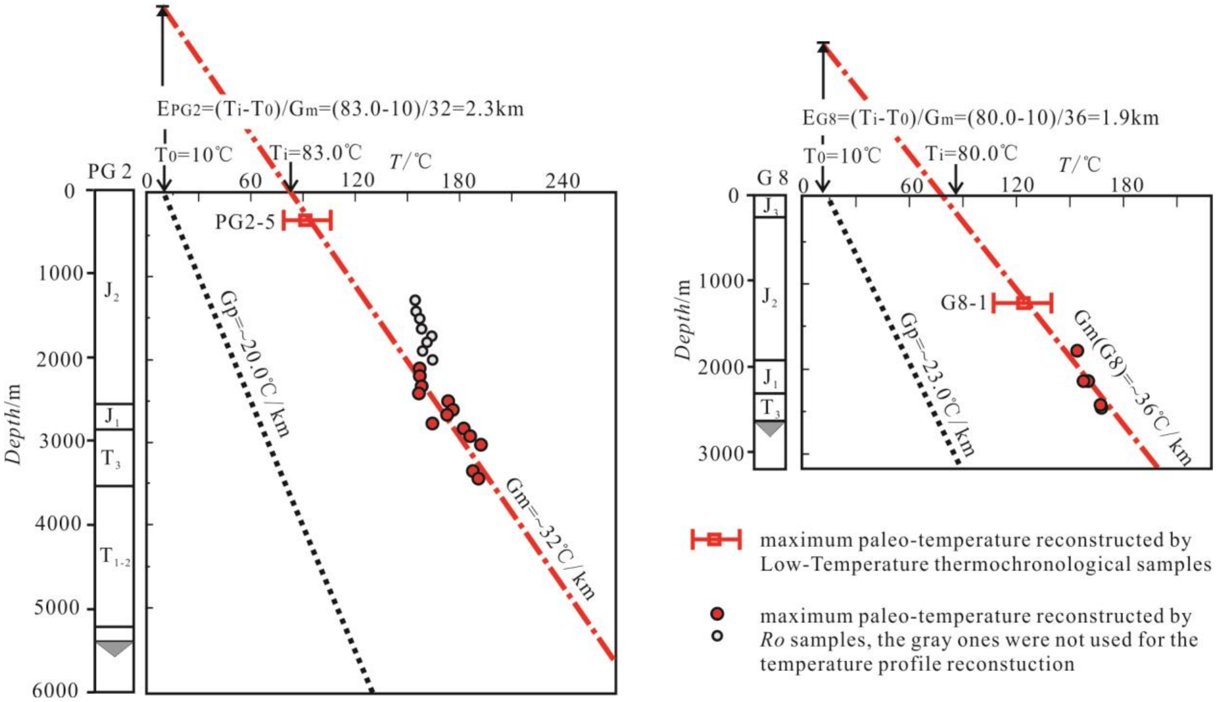

Fig. 9 Maximum paleogeothermal profiles reconstruction of PG2 and G8 in the Eastern Sichuan Basin. The maximum paleotemperature gradients (Gm) are calculated using the maximum paleotemperatures that are reconstructed based on the Ro and low-temperature thermochronology data via a thermal history modeling software "Thermodel for Windows 2008" which is developed and managed by Prof Shengbiao Hu (website: http://www.thermodel.com). The EASY%Ro model (Sweeney and Burnham, 1990) was employed to reconstruct the maximum paleotemperatures from Ro data.

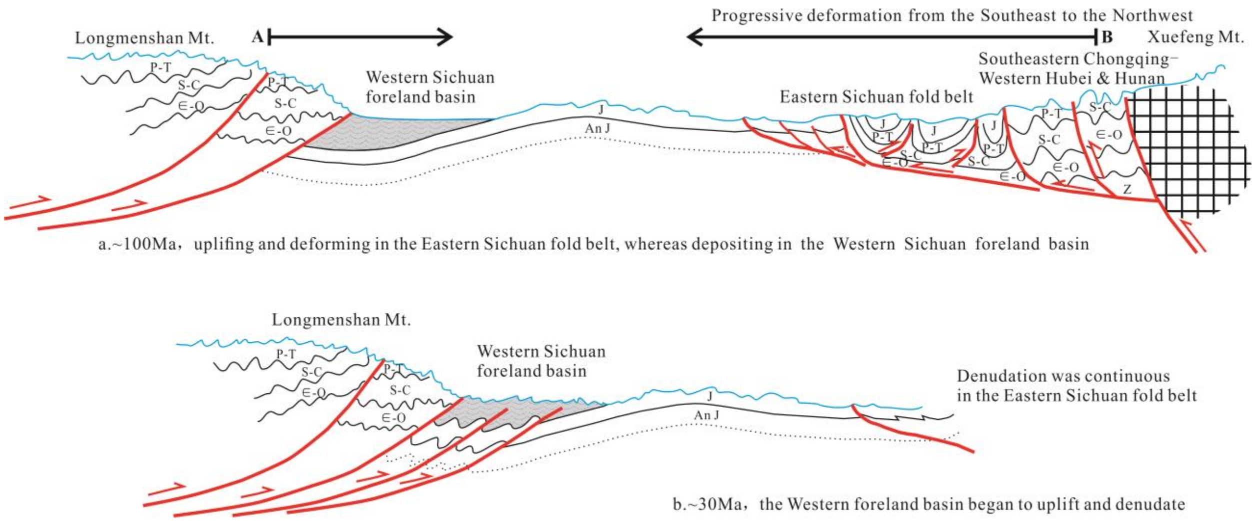

Fig. 10 Simple model shows the different denudation process between the Eastern and Western Sichuan Basin